AGU ADVANCING EARTH AND SPACE SCIENCE

Space Weather

RESEARCH ARTICLE
10.1029/2019SW002378

Key Points:
- Rate of total electron content change, HF, and UHF auroral backscatter revealed similar dynamics during geomagnetic storm
- UHF/HF auroral backscatter appeared/disappeared almost simultaneously with field-aligned currents and particle precipitation increase/decrease
- Configuration of R1/R2 field-aligned currents influence on horizontal and vertical transport of ionospheric irregularities

Supporting Information:
- Supporting Information S1
- Movie S1
- Movie S2
- Movie S3
- Movie S4
- Movie S5

Correspondence to:
M. V. Klimenko,
maksim.klimenko@mail.ru

Citation:
Ovodenko, V. B., Klimenko, M. V., Zakharenkova, I. E., Oinats, A. V., Kotova, D. S., Nikolaev, A. V., et al. (2020). Spatial and temporal evolution of different-scale ionospheric irregularities in Central and East Siberia during the 27–28 May 2017 geomagnetic storm. *Space Weather*, *18*, e2019SW002378. https://doi.org/10.1029/2019SW002378

Received 14 OCT 2019
Accepted 13 MAY 2020
Accepted article online 19 MAY 2020

Spatial and Temporal Evolution of Different-Scale Ionospheric Irregularities in Central and East Siberia During the 27–28 May 2017 Geomagnetic Storm

V. B. Ovodenko[1], M. V. Klimenko[1], I. E. Zakharenkova[1], A. V. Oinats[2], D. S. Kotova[1,3], A. V. Nikolaev[4], I. V. Tyutin[5], D. D. Rogov[4], K. G. Ratovsky[2], D. V. Chugunin[1,6], P. A. Budnikov[7], J. C. Coxon[8], B. J. Anderson[9], and A. A. Chernyshov[1,6]

[1]West Department of Pushkov Institute of Terrestrial Magnetism, Ionosphere and Radio Wave Propagation, RAS, Kaliningrad, Russia, [2]Institute of Solar Terrestrial Physics, SB RAS, Irkutsk, Russia, [3]Department of Physics, University of Oslo, Oslo, Norway, [4]Arctic and Antarctic Research Institute, Saint-Petersburg, Russia, [5]JSC Scientific Research Institute for Long Distance Radiocommunication, Moscow, Russia, [6]Space Research Institute of the Russian Academy of Science, Moscow, Russia, [7]Fedorov Institute of Applied Geophysics, Moscow, Russia, [8]University of Southampton, Southampton, UK, [9]Johns Hopkins University Applied Physics Laboratory, Laurel, Maryland, USA

Abstract We present a multi-instrumental study of ionospheric irregularities of different scales (from tens of centimeters to few kilometers) observed over the Central and East Siberia, Russia, during a moderate-to-strong geomagnetic storm on 27–28 May 2017. From high-frequency (HF) and ultrahigh-frequency (UHF) radar data, we observed an intense auroral backscatter developed right after the initial phase of the geomagnetic storm. Additionally, we examined variations of Global Positioning System (GPS)-based ROT (rate of TEC changes, where TEC is total electron content) for available GPS receivers in the region. Ionosondes, HF, and UHF radar data exhibited a presence of intense multi-scale ionospheric irregularities. We revealed a correlation between different-scale Auroral/Farley-Buneman ionospheric irregularities of the E layer during the geomagnetic storm. The combined analysis showed that an area of intense irregularities is well connected and located slightly equatorward to field-aligned currents (FACs) and auroral oval at different stages of the geomagnetic storm. An increase and equatorward displacement of Region 1 (R1)/Region 2 (R2) FACs leads to appearance and equatorward expansion of ionospheric irregularities. During downward (upward) R1 FAC and upward (downward) R2 FAC, the eastward and upward (westward and downward) E × B drift of ionospheric irregularities occurred. Simultaneous disappearance of UHF/HF auroral backscatter and GPS ROT decrease occurred during a prolonged near noon reversal of R1 and R2 FAC directions that accompanied by R1/R2 FAC degradation and disappearance of high-energy auroral precipitation.

1. Introduction

In the high-latitude ionosphere, intense ionospheric irregularities and plasma structures with characteristic scales from small (centimeter level) to large scale (>10 km) can be formed during magnetospheric storms and substorms due to two-stream (Farley-Buneman) (Buneman, 1963; Farley, 1963) and gradient-drift plasma instabilities (e.g., Rogister & D'Angelo, 1970). The main conditions supporting the plasma instabilities are the presence of a strong electric field, high electron velocity relative to ions, and presence of sharp plasma density gradients. High-latitude ionospheric irregularities are field-aligned plasma structures (Kelley, 2009).

A significant feature of such irregularities is that they scatter and reflect radio waves. That is, why these irregularities were well investigated by coherent radars in high-frequency (HF), very HF, ultrahigh-frequency (UHF), and L bands (Fejer & Kelley, 1980; Leadabrand et al., 1967; Schlegel, 1996) and by incoherent radars (Foster & Tetenbaum, 1991; Uspensky et al., 2011). Previous studies of radar auroral backscatter allow to list the main characteristic of these phenomena (see reviews of Cole, 1963; Fejer & Kelley, 1980; Hanuise, 1983; Haldoupis, 1989; Greenwald, 1996; Hysell, 2015). An altitude of scattering is 100–130 km which coincides with the altitude placement of the auroral electrojet. We note that radar observations can provide an approximate upper bound on the irregularity thickness in the range from

2.5 to 20 km (Leadabrand et al., 1965; Unwin, 1966). The amplitude of backscattered signal depends on the auroral electrojet intensity (Greenwald et al., 1973; Uspensky et al., 1989) and electron density (Starkov et al., 1983). Auroral backscatter was observed under conditions of strong electric field of 10–30 mV/m (Hysell et al., 2012; Koustov et al., 1989; Tsunoda & Presnell, 1976). Signal energy backscattered from plasma irregularities decreases strongly when the angle between the wave vector and the normal of the magnetic field direction (aspect angle) changes from its zero value, so-called aspect angle sensitivity (Leadabrand et al., 1967; McDiarmid, 1976; Moorcroft, 1996; Schlegel & Gurevich, 1997). Theory reported by Buneman (1963) and Farley (1963) explained field-aligned nature of electrojet irregularities.

There are papers devoted to investigate optical aurora and radar backscatter (Bagaryatsky, 1961; Bahcivan et al., 2006; Cole, 1963; Jayachandran et al., 2002; Prikryl & Cogger, 1992; Tsunoda & Presnell, 1976). Most of these studies have suggested that there exists a relationship between the radio and discrete optical aurora, but they were not co-located (Hysell et al., 2012; Tsunoda & Presnell, 1976). In general, the radar backscatter is observed equatorward of the active optical aurora in the eastward electrojet region (dusk-midnight sector) (Cole, 1963; Jayachandran et al., 2002; Prikryl & Cogger, 1992; Tsunoda & Presnell, 1976). The radar backscatter was often observed at the discrete arc boundary and suppressed inside the arc (Bahcivan et al., 2006). On the other hand, some of the brightest optical aurorae are found coincident with the strongest radar backscatter power (Bahcivan et al., 2006; Jayachandran et al., 2002; Prikryl & Cogger, 1992). We note that many radars used in experiments have range resolution seldom better than 6 km; therefore, such estimates are approximate.

An attempt of joint analysis of auroral backscatter and field-aligned currents (FACs) was undertaken by Sverdlov et al. (1979). The same topic was discussed by Kamide and Rostoker (1976), Tsunoda and Presnell (1976), and Kamide (2013). According to global distributions of auroral backscatter and FAC gathered from Triad satellite data, it was shown that radar aurora and R2 FAC have a close location. However, the description of the global distribution of FAC was carried out only schematically due to limitations in temporal and spatial resolution of data. Sverdlov et al. (1979) and Gustafson et al. (1980) discussed the role of FAC in meter-scale irregularities formation based on experimental data. However, none of these articles demonstrated a detailed comparison of the temporal development of auroral backscatter and FAC. One of the goals of our investigation is to demonstrate a link between temporal dynamics of the magnetosphere-ionosphere FACs and different-scale ionospheric irregularities developed during geomagnetic storms.

During the last decades, regular measurements of radio signals of the Global Positioning System (GPS) have been used actively to investigate and to monitor the ionospheric irregularities occurrence (e.g., Aarons & Lin, 1999; Cherniak et al., 2019; Jakowski et al., 2012; Prikryl et al., 2016). At high latitudes, phase scintillations substantially prevail over amplitude ones (e.g., Prikryl et al., 2014). To characterize phase scintillations level, there are commonly used the phase scintillation indexes σ_{φ} and ROTI (rate of TEC change index, where TEC is total electron content). Earlier studies demonstrate that ROTI allow to describe spatial-temporal characteristics of irregularities during geomagnetic storms and can represent the auroral oval dynamics (e.g., Cherniak et al., 2015). However, one of the main limitations of the GPS technique is the impossibility to determine an altitude or altitudinal extent where ionospheric irregularities occur along the line of site between a ground-based receiver and a GPS satellite. Only a combination with concurrent measurements from other instruments can provide clues on the altitudinal distribution of the ionospheric irregularities detected by GPS receivers. Also, an interrelation between GPS ROTI and auroral backscatter at different bands has not been studied yet.

In the paper we investigate the behavior of ionospheric irregularities with scales from tens of centimeters to few kilometers in spatial and temporal domain using comprehensive set of space- and ground-based instruments. We focus on investigation of the HF and UHF auroral backscatter and its possible relationship to (1) the storm-induced auroral ionospheric irregularities as detected in GPS observations and (2) magnetospheric energy inputs to the upper atmosphere and ionosphere that characterized by FACs and auroral particle precipitation. Usage of a multi-instrumental (GPS, UHF and HF radars, ground-based ionosondes, riometer, and AMPERE FACs) and multi-point database for the Central and East Siberian region provides us with an excellent and unique opportunity to investigate these interrelations in detail for a case study of the 27–28 May 2017 geomagnetic storm.

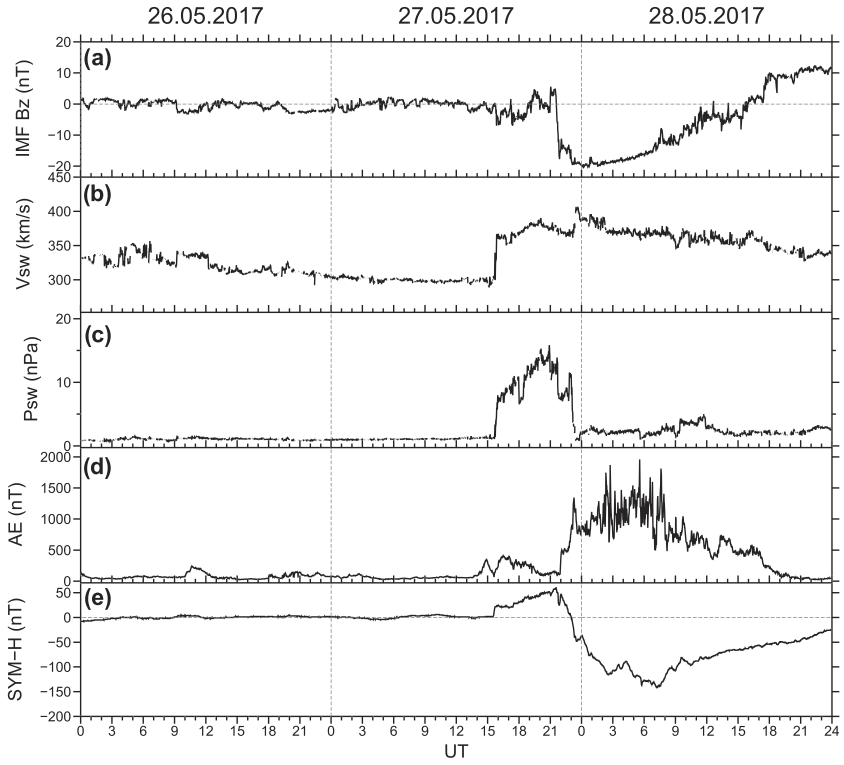

Figure 1. Variations of (a) IMF Bz component, (b) solar wind velocity and (c) pressure, the geomagnetic indices (d) AE, and (e) SYM-H during 26–28 May 2017. All data are 1-min-averaged data from the OMNIWeb service.

2. Geomagnetic Storm Description

A moderate-to-strong geomagnetic storm according to NOAA scales occurred on 27 May 2017 at 15:34 UT. Figure 1 shows the interplanetary magnetic field (IMF) and geomagnetic conditions during 26–28 May 2017 (from OMNIWeb service, https://omniweb.gsfc.nasa.gov/form/omni_min.html). This storm has a prolonged initial phase (~6 hr) from 15:30 to 21:30 UT on 27 May 2017. The solar wind speed changed from ~300 to ~360–370 km/s; however, the storm was characterized by a prolonged period of steady southward IMF Bz and intense geomagnetic activity. The main phase developed from 22:05 UT on 27 May till 07:16 UT on 28 May 2017 when the SYM-H index (1-min resolution Dst) reached its minimal excursion of −142 nT. The steady southward IMF Bz was observed from 21:35 UT on 27 May till ~12–13 UT on 28 May 2017 — during this period the auroral electrojet (AE) index reached its maximal values. The AE index had peak values of ~1,500–1800 nT during 03–09 UT on 28 May 2017. The recovery phase began after 07 UT on 28 May 2017 and lasted till 30 May 2017.

3. Observation Data

We used a comprehensive set of radiophysical instruments that provided us an opportunity to investigate the ionospheric plasma density irregularities of different scales. Figure 2 shows the geographical map with locations of all involved radiophysical instruments. To investigate mechanisms responsible for ionospheric irregularities generation and evolution, we used data of FACs collected by satellites, energy, and number fluxes of auroral precipitation obtained from the modified OVATION Prime empirical model.

As one can see from Figure 2, instruments cover a huge area in Central and East Siberia, Russia. The HF (EKB) and UHF (KNK) radars can detect echoes only in a limited area which is determined by geometric conditions of intersection radar beam and altitude of the E layer and F layer in case of HF radar. East azimuthal beam directions correspond to lower latitudes for both radars. The ground-based GPS stations AMDE (Amderma), SALE (Salekhard), SEYA (Seyakha), and NRIL (Norilsk) are the nearest ones to the

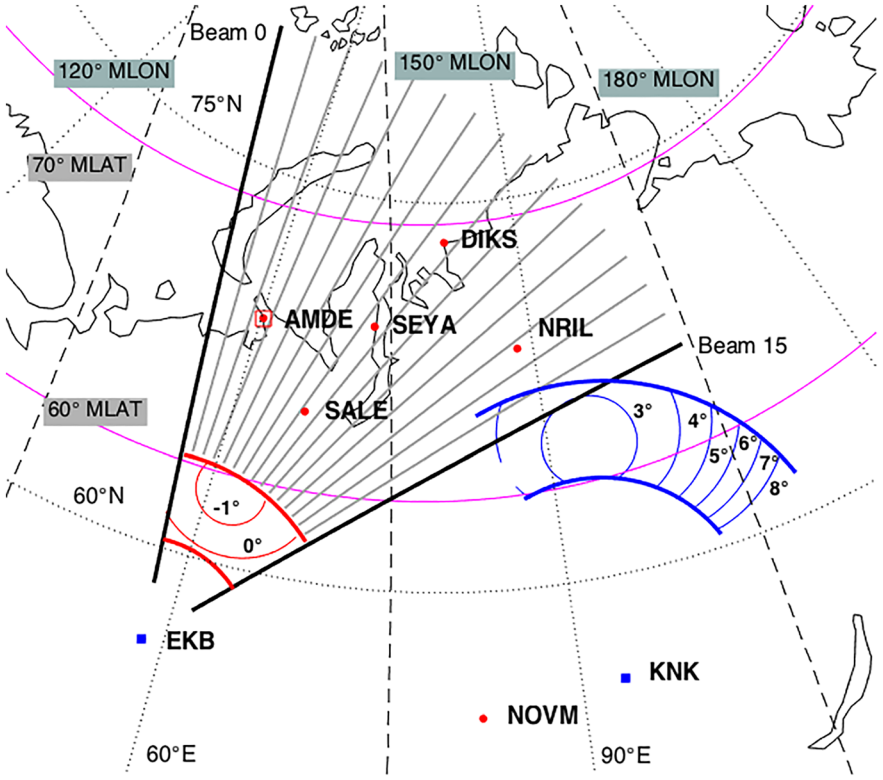

Figure 2. Locations of geophysical instruments in geographical coordinates. A part of the UHF radar field of view responsible for detecting irregularities at the ionospheric E layer altitude is shown by two blue arcs indicating altitude of 70 and 150 km (equivalent range 700 and 1,100 km). The full field of view of the HF radar is shown by black lines indicating 16 radar beams faced at different azimuthal directions. Solid lines inside UHF and HF field of view indicate the aspect angle loci for altitude of 110 km. Red dotted lines inside HF radar field of view indicate an area of signal backscattering at the first hop. The GPS receiver locations are shown by red circles and four-letter names. The radar locations are shown by blues squares and three-letter names. There are also co-located ionosonde indicated by red square at the AMDE site.

HF and UHF radar's field of view. Radars can detect ionospheric irregularities at the following latitudinal ranges: 58–63°N (EKB HF radar) and 61–68°N (KNK UHF radar). Ground-based GPS receivers collect signals from several GPS satellites in view; GPS ionospheric piercing point projections cover an area of ~10° in average around a receiver's location. To indicate a latitudinal extent of ionospheric irregularities, DIKS (Dikson) and NOVM (Novosibirsk) stations were also considered as the most northern and southern borders. Both receivers are located within approximately the same longitudinal sector as the NRIL station. All the data used presented in altitude adjusted corrected geomagnetic coordinates.

3.1. UHF Radar

We considered data collected by the UHF radar (440 MHz) to study a temporal and spatial behavior of the ionospheric irregularities of the E layer. The radar has a poleward field-of-view orientation and is located near Krasnoyarsk (KNK) area (56°N, 93°E); see Figure 2. The radar cover ranges from 700 to 2,000 km in azimuthal sector of 80° with a fixed elevation angle of ~3°. The measured radar parameters are range, elevation, azimuth, and signal-to-noise ratio (SNR). Doppler velocity measurements are not available. During its operation, the radar is scanning by azimuth every 10 s. The radar allows to detect echoes with altitude resolution of about 1 km using monopulse feed. Radar can reliably detect an ionospheric scatter −50 decibels-relative-to-square-meter (dBsm) at a range of 100 km.

We analyzed data with altitude of 70–150 km. The echoes with altitude range of 90–130 km are corresponded to radar auroral backscatter; see, for example, Leadabrand et al. (1965). Rare echoes at altitudes of

70–150 km are considered as a specular scattering from meteor trails or their heads. We note that the UHF radar can detect coherent echoes from the field-aligned irregularities whose size (~40 cm) is half of the radar wavelength. The minimum observable aspect angle is about 3°, and radar observations cover a range of magnetic aspect angles up to 9°.

3.2. HF Radar

The EKB HF radar is located in Arti (56.4°N, 58.5°E) of Sverdlovskaya region (see Figure 2). According to the technical characteristics, the EKB radar is similar to the radars within the SuperDARN (Chisham et al., 2007). The EKB antenna forms narrow pattern with a beam width of 3.5° in azimuth, called "beam." The beam can be focused in 16 azimuthal directions separated by 3.24°. The westernmost beam (#0) and the easternmost beam (#15) have azimuths of −4.3° and 44.3°, respectively. In standard operational mode the radar sequentially transmits and receives HF waves in each of the directions. The measured characteristics are the slant range, Doppler velocity, and spectral width, as well as the SNR of the received echoes. The slant range varies from about 100 to 3,500 km. The EKB radar has two channels that can perform transmission and receiving signal independently. During 27–28 May EKB radar operated at all of 16 beams in Ch. #1 at frequency of 11.3 MHz, and at three beams #0, #1, and #2 in Ch. #2 at frequency of 10.8 MHz. Time resolution was about 2 min and about 20 s in Ch. #1 and Ch. #2, respectively. The radar waveform was standard for SuperDARN, and the slant range resolution was 45 km. Elevation angle measurements are not provided by the EKB radar during the period under consideration.

The Doppler velocity and spectral width registered by the radar allow us to identify a scatter type. The above characteristics are typically small for ground scatter (some exclusion presented by Jayachandran et al., 2000), since ground surface remains stationary during signal duration. On the contrary, velocity and spectral width for ionospheric scatter are typically significantly higher. The above assumption is taken into account in standard empirical criterion (Blanchard et al., 2009) for separation of ionospheric echoes from ground scatter echoes. As indicated in several studies (see, e.g., Nishitani et al., 2019), this criterion works reasonably well for high-latitude HF radars. At midlatitudes, ionospheric plasma convection velocity can be comparable to the magnitude of Doppler velocity expected for ground scatter. For this reason, in addition to the standard criterion, we also analyzed the slant range of the echoes in order to get more accurate echo type identification (Oinats et al., 2016). The size of ionospheric irregularities that can be detected by the radar as coherent echo is equal to the half of operational wavelength, that is, about 15 m. For the HF EKB radar the observable aspect angles are from 0° to 1° (see Figure 2).

3.3. Ionosondes and Riometer

The measurements provided by an ionosonde and riometer located in Amderma (69.60°N, 60.20°E) were also used for our study. These instruments are a part of the Arctic and Antarctic Research Institute (AARI, St. Petersburg) high-latitude ionospheric observation network. Vertical ionospheric sounding instrument is designed to study the ionospheric layers parameters by constructing the height-frequency characteristics of the ionospheric plasma above the ionosonde equipment. Canadian Advanced Digital Ionosonde (CADI) was installed at the Amderma location. Operation mode is every 15 min. The results of automatic processing of ionograms are often incorrect in high-latitude ionosphere; thus, all ionograms were interpreted manually by experienced scalers. The riometer is a cosmic radio noise receiver. It is an effective tool for the high latitudinal lower ionosphere investigating. A standard wide-beam riometer (with a beam width of about 60°) at 30 MHz is also installed at the Amderma station.

3.4. GPS Receivers

Ionospheric irregularities can affect both amplitude and phase of the received GPS radio signal. To probe the phase fluctuation activity, there are ROT (rate of TEC change) and ROTI (rate of TEC change index) indicators that were initially proposed by Pi et al. (1997) and are now used for detection and characterization of the ionospheric irregularities occurrence on regional and global scales. So GPS observations can provide information on occurrence and severity of ionospheric irregularities, but not about altitudinal location or extent of these structures. It is generally believed that small-scale (<300–400 m) plasma irregularities within the ionospheric F2 layer contribute the most to amplitude scintillations of GPS signals, whereas ionospheric plasma structures with a larger scale can cause rapid changes of navigation signal carrier phase. In fact, ROT is considered as a measure of changes of ionospheric delay between two

epochs. We calculated ROT value as a time derivative of slant relative TEC values at a 30-s interval and ROTI as a standard deviation of ROT at a 5-min interval for all visible GPS satellites with an elevation above 25°. During pre-processing, all GPS data were uniformly resampled to a 30-s rate. Here, we processed GPS observations from several ground-based GPS stations located in Eastern and Central Siberia (see Figure 2 for locations and Figure 5 for coordinates and names of all receivers). Note that we involved all available GPS observations at this part of Russia. Using GPS data, we can observe kilometer-scale ionospheric irregularities.

3.5. AMPERE Field-Aligned Currents

The Active Magnetosphere and Planetary Electrodynamics Response Experiment (AMPERE) data were used to investigate the dynamics of the Birkeland currents using magnetometer measurements of the Iridium satellite network (Anderson et al., 2014). AMPERE data allow to globally examined the Region 1 and Region 2 FACs structure and their temporal evolution. The Iridium constellation consists of 66 satellites in the communications network together with on-orbit spares, which orbit the Earth in six circular, polar, orbital planes at an altitude of 780 km and a longitudinal spacing of ~2 hr of MLT (Murphy et al., 2013). There are 11 satellites per orbital plane in the Iridium network, and each orbit has a period of 104 min, such that it takes a satellite 9.5 min to move from its current position to the current position of the next satellite. The magnetometer data from the Iridium are used in AMPERE to derive the Birkeland current (that assuming to be radial) density making use of Ampère's law. Data are composed of a series of 10-min windows, evaluated every 2 min, and presented on a grid of resolution 1° latitude and 1 hr of MLT. AMPERE data are presented in altitude adjusted geomagnetic (AACGM) coordinates at an altitude of 780 km. More detailed information about AMPERE methodology of Birkeland current observation and obtained scientific results were presented in a recent review by Coxon et al. (2018). Note that there is a small data gap in AMPERE data from 23:57 UT on 27 May to 0:17 UT on 28 May 2017.

3.6. Auroral Particles Precipitation by OVATION Prime Model

In order to indicate auroral particles precipitation, we use the OVATION Prime (2010) model (hereinafter referred as OP-2010), which was initially developed by P. T. Newell and his colleagues at the John Hopkins University Applied Physics Laboratory (JHU/APL), because it has several key advantages over the other models: (1) It separately categorizes both the discrete (electrons) and diffuse (electrons and ions) aurora (Newell et al., 2009); (2) it calculates auroral power and auroral oval boundaries for low and moderate magnetospheric activity (Kp < 5+) (Newell et al., 2010) better than, for example, the Evans nowcast model (Evans, 1987), Hardy Kp-Based Model (Hardy et al., 1985, 1989); and (3) it empowers more detailed information about particles precipitation areas covering the whole auroral zone in 50–90° geomagnetic latitude (MLAT) interval with (0.25 h MLT × 0.5° MLAT) grid resolution.

Basically, the OP-2010 has been developed on the basis of statistical relationship between particle precipitations observed by DMSP spacecraft and Solar Wind (SW) parameters (v—SW velocity, B_t—tangential IMF component, and θ_c—IMF tangential component clock angle) obtained from the ACE spacecraft. The combination of these SW parameters was introduced to the model in a form of the Newell's function:

$$\mathrm{N}(v, B_t, \theta_c) = v^{4/3} \cdot {B_t}^{2/3} \cdot \sin^{8/3}(\theta_c/2) \quad (1)$$

which serves as the main input parameter. For the purposes of our study, N was replaced with the PC index (Troshichev et al., 1988; Troshichev & Andrezen, 1985) through the use of multivariable regression in a form of

$$\mathrm{N}\,(\mathrm{PC}, \Delta\mathrm{PC}_5, \Delta\mathrm{PC}_{10}) = \mathrm{k}_1 \cdot \mathrm{PC} + \mathrm{k}_2 \cdot \Delta\mathrm{PC}_5 + \mathrm{k}_3 \cdot \Delta\mathrm{PC}_{10} + \mathrm{k}_4 \quad (2)$$

(where $\Delta\mathrm{PC}_5$ and $\Delta\mathrm{PC}_{10}$ are the PC-index changes at 5- and 10-min time scales) because the PC index can be considered as an indicator of the SW energy that already penetrated into the magnetosphere, while the function N indicates energy that only may penetrate to it. Thus, a nowcasting ability of the original OP-2010 model was improved as its preliminary was shown by determination coefficients ${R^2}_{\mathrm{PC}} \sim 0.52$ and ${R^2}_{\mathrm{N}} \sim 0.52$ derived from auroral power predictions (for both model versions) compared to Polar UVI observations.

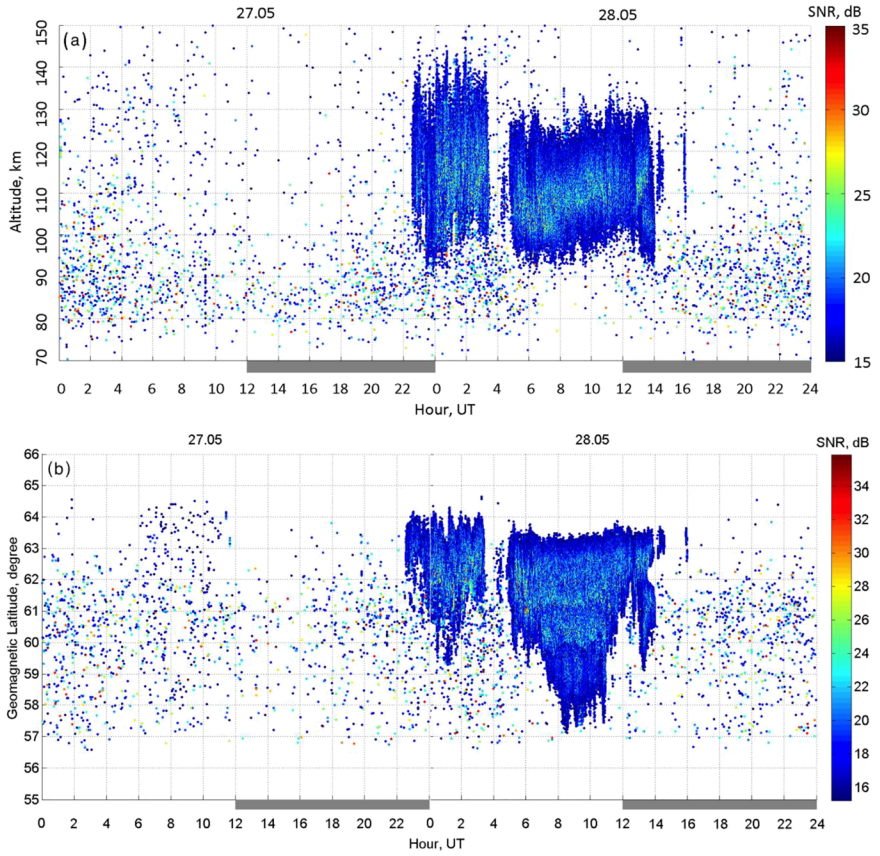

Figure 3. Altitude-time-SNR (a) and geomagnetic latitude-time (b) dependence of echoes observed by UHF radar during 27–28 May 2017. Color bar indicates signal-to-noise ratio (in decibels) of echoes. Gray shadow below each graph shows 18–06 MLT conditions.

4. Results

4.1. UHF Radar

Altitude-time-SNR and geomagnetic latitude-time dependencies of auroral radar backscatter characterizing 40-cm irregularities for 27–28 May 2017 are provided in Figure 3. Analysis of radar echoes revealed that geomagnetic latitude of intense radar echoes varies from 59.5–64.5°N during the main phase of geomagnetic storm (from 22:30 on 27 May till 03:30 UT on 28 May) to 57.0–63.5°N at the latter stage of storm development (from 05:00 till 14:00 UT on 28 May). There is a significant altitudinal difference between the first (95–140 km from 22:30 on 27 May till 03:30 UT on 28 May) and second (95–125 km from 05:00 till 14:00 UT on 28 May) block of UHF radar backscatter. In general, such altitude ranges of observed radio aurora are in good agreement with the previous studies; see, for example, Leadabrand et al. (1961). There are also echoes at altitudes of 70–150 km which are backscattered signals from ionized meteor trails and their heads. The SNR maximum at an altitude of 110 km is more probably explained by maximum of the electron density at E layer. Out of this altitude range SNR is 15–20 dB in average. Such SNR variability was observed by STARE radars earlier by Uspensky et al. (2011) and explained mainly as a variability of the electron density.

A sharp increase of radar echoes was observed at about 22:30 UT on 27 May. A continuous increasing of the latitude range of auroral backscatter was observed from 22:30 UT on 27 May (62.5–64.0°N) until 01:00 UT on 28 May (59.5–64.0°N). After that the decreasing of latitudinal range of radar aurora were observed until about 03:30 UT on 28 May. Then intense echoes disappeared from 03:30 UT until about 05:00 UT on 28 May. This period approximately corresponds to conditions of magnetic noon and the reverse of the FACs and ionospheric electrojet flow.

Intense echoes appeared again at 05:00 UT with latitudinal range of 60.0–63.5°N, and continuous increasing of the latitude range of auroral backscatter was observed until 08:30 UT on 28 May (57.0–63.5°N). The largest latitudinal range of auroral backscatter was observed during time interval 8:30–11:00 UT on 28 May. After that the decreasing of radar aurora latitudinal range (62–63.5°N) were observed until 13:00 UT on 28 May 2017. A very sharp equatorward expansion of radar aurora (down to 59.5°N) was observed from 13:00 UT till 13:30 UT on 28 May. During 13:30–14:00 UT on 28 May, two phenomena occurred: (1) a sharp poleward displacement of radar aurora to 60.5°N at 14:00 UT and (2) a clear two-branch structure of echoes with a gap in latitude. Radar aurora disappeared after 14:00 UT.

The temporal development of latitude-longitude dependence of echoes from 16:00 UT on 27 May until 15:00 UT on 28 May presented as a movie at supporting information (see Movie S1). The two arcs on a movie indicate the lowest and highest altitude border of area where auroral radar backscatter could exist. The spatial structure of echoes (irregularities) changes fast enough as seen with high time resolution of 1 min and could not be explained as a regular shape. Though in general the appearance of echoes is structured in azimuthal direction and has a variable strength in range (altitude).

Intense radar echoes exist not in all radar field of view during the considered time interval of 27–28 May 2017. Auroral backscatter started to appear at 67°N latitude at the west azimuthal directions covering the longitudinal range from 85°E to 95°E at 22:30 UT on 27 May. Eastward and therefore equatorward expansion of radar aurora was occurring until 01:30 UT on 28 May when auroral echoes covered a longitudinal range of 84–105°E. Intense auroral backscatter was absent during 03:30–04:50 UT on 28 May. Auroral backscatter started to appear again at 65–67°N at the central azimuthal directions covering the longitudinal range from 95°E to 100°E at 04:50 UT on 28 May. The primarily westward and at the some moments equatorward expansions of radar auroral backscatter occur until 07:00 UT on 28 May when auroral echoes covering the longitudinal range 84–105°E. A continuous expansion of auroral backscatter toward east azimuthal direction and therefore equatorward was started at 07:00 UT on 28 May. This expansion is well seen in Figure 3b as a spreading of echoes toward their lowest latitudes at ~57° MLAT. Intense radar echoes exist almost in all radar field of view during 08:00–11:00 UT on 28 May covering longitudinal range of 84–108°E. Thus, the most latitudinally expanded auroral backscatter was observed during time interval 08:00–11:00 UT on 28 May. A clear two-branch structure of echoes was observed during 13:30–14:00 UT on 28 May during the recovery storm phase. The poleward branch is observed at geographical latitudes of 66–67.5°N and the equatorward branch observed at latitude range of 64–65.5°N.

4.2. HF Radar

Figure 4 presents the EKB HF radar data recorded on 27–28 May 2017. There is also a similar figure in the supporting information which shows the data from 18 UT on 27 May till 06 UT on 28 May 2017 in more detail. Figure 4a presents the range-time-SNR plot for the Beam #2 (Ch. #2). Figures 4b, 4d, and 4e show latitude-time dependencies of SNR, Doppler velocity, and spectral width for the Beam #2 (Ch. #2). Figure 4 shows only the echoes with SNR greater than 3 dB to avoid noisy picture. The Beam #2 azimuth is equal to a value of about 2.2° that corresponds to a direction toward the Amderma station. Thus, for comparison reasons, we also present an absorption (in decibels) level with respect to quiet day curve and critical ionosphere frequencies (foF2, foE, foEs, and fmin) for the Amderma station on Figures 4c and 4f, respectively. Panel 4g shows the latitude-time-velocity plot for the Beam #12 (Ch. #1) directed toward Norilsk. Panel 4g shows only the echoes with SNR greater than 1 dB to avoid noisy picture. The minimum frequency (fmin) at vertical sounding (VS) is determined by radio waves absorption, as well as the parameters of the receiver, transmitter, the antenna-feeder system, and the overall noise situation at the station. Nevertheless, the comparison of fmin by VS and absorption by riometer gives a good agreement between these parameters.

In Figure 4a, black and gray solid curves show slant range dependencies corresponding to diurnal variations of the HF skip distance for the ionospheric F2 and E layers HF channels, respectively. These dependencies were calculated by the technique (Kurkin et al., 2012) developed in the ISTP SD RAS using the IRI-2012 ionospheric median model (Bilitza et al., 2014). The solid curves show the smallest possible slant range for ground scatter echoes for undisturbed conditions on a given day, operational frequency, and radar beam. The echoes lying on the figure below the solid curves should be interpreted as ionospheric scatter echoes regardless their Doppler velocity and spectral width values. The above criteria are used for a

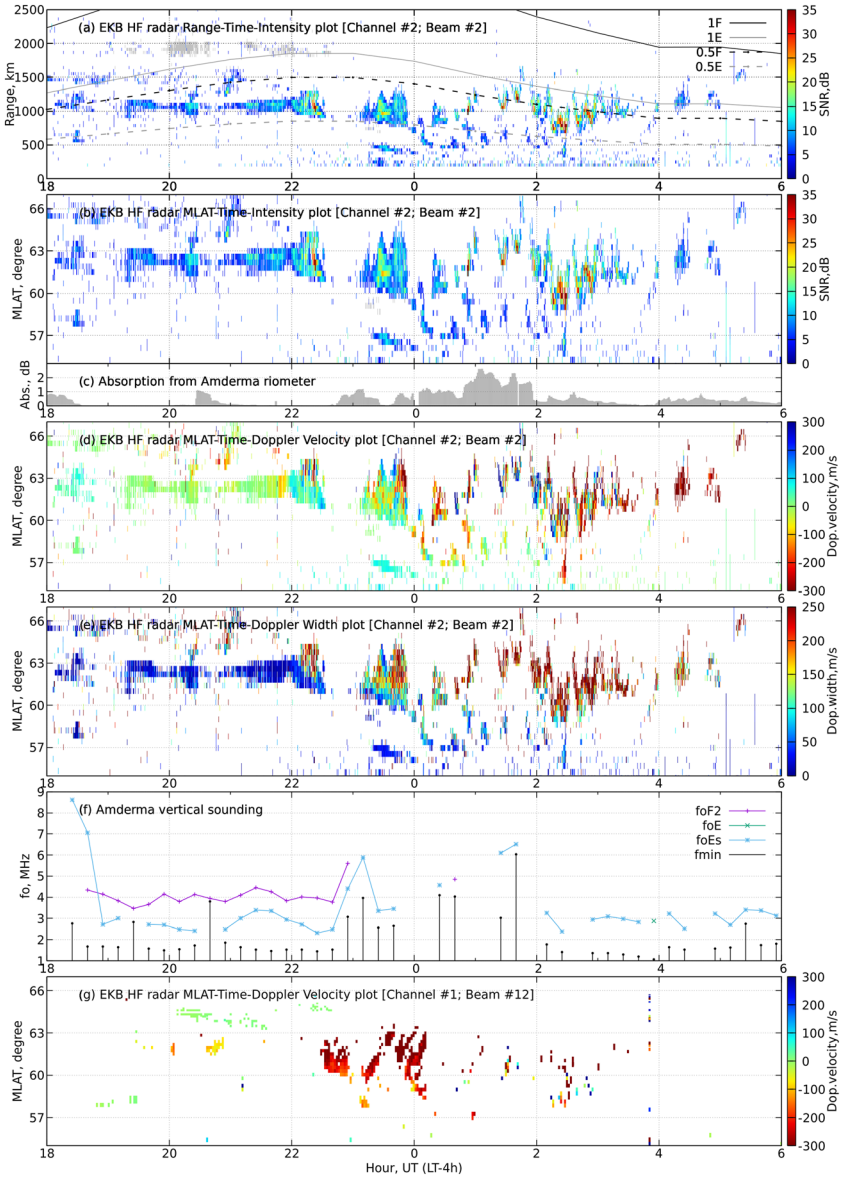

Figure 4. The EKB HF radar observations during 27–28 May 2017: (a) the range-time-SNR plot for the Beam #2 (Ch. #2); (b, d, and e) the latitude-time plots for SNR, Doppler velocity, and spectral width for the Beam #2 (Ch. #2); (c) the absorption in decibel from Amderma riometer; (f) the critical frequencies (foF2, foE, foEs, and fmin) from the Amderma vertical sounding station; and (g) the latitude-time-velocity plot for the Beam #12 (Ch. #1).

differentiation of echoes of ground and ionospheric origin in addition to the standard approach (Blanchard et al., 2009). The dependencies of slant ranges to ionospheric reflection region are shown by black and gray dashed lines corresponding to the skip distance. These dependencies are used for echoes mapping (Oinats et al., 2016).

The ground scatter is shown by gray color on Figures 4a and 4b. Echoes with a slant range less than ~200 km are signals backscattered from meteors (Chisham & Freeman, 2013), and ionospheric scatter is shown by color according to the right-side color box. The red/blue color on Figure 4d corresponds to the echoes propagating in the opposite/direct direction to the radar. Note that starting from 04 UT on 28 May 2017, the EKB radar was operated according to the specific schedule, when the standard operational scan mode had been switched on only twice per hour during 15 min at 15th and 45th minute of every hour. Starting from ~18:00 UT on 27 May and till to ~05:30 UT on 28 May 2017, a strong coherent scatter from the ionospheric irregularities was observed at slant ranges of 700–1,500 km. As seen from Figure 4f, this time period

coincides with the Es layer observation at the Amderma station. The Es layer critical frequency (foEs) varies from 2.3 to 8.6 MHz during this period. Thus, we assume that the observed coherent scatter comes from the E layer heights. According to the scatter characteristics, we divide the period into three intervals.

The first interval is 18:00–22:00 UT on 27 May 2017. It corresponds to the moderate geomagnetic activity as seen from Figure 1. Ionospheric scatter for this interval represents an almost continuous trace in time domain. Doppler velocities vary from −80 to 80 m/s, spectral width is about 10 m/s, and SNR is about 12 dB. Slant range varies from 1,000 to 1,200 km, and corresponding geomagnetic latitude is about 62° MLAT. Absence of radar echo is seen from 18:30 till 19:15 UT and at ~20:40 UT on 27 May. The absence intervals partially coincide with enhanced absorption in the lower ionosphere (D and E region) as confirmed by the riometer data and by fmin variations measured at the Amderma station (see Figures 4c and 4f).

The second interval is 22:00–24:00 UT on 27 May. This interval corresponds to the phase of sharp changes in all indices shown on Figure 1. Ionospheric scatter during this interval is also relatively continuous in time domain, but it is extended along a slant range from 800 to 1,400 km. The lowest scatters latitude is not stable; it changes from 62° at the beginning to ~59° MLAT at the end of temporal interval. Doppler velocity varies in the range from −300 to 250 m/s, the spectral width is from 10 to 250 m/s, and SNR reaches up to 30 dB. There is a long period of echoes absence from ~22:30 till 23:20 UT. The absence period coincides with the increase in absorption and fmin as also seen from Amderma ionosonde and riometer.

The third interval is from 00:00 UT till 05:30 UT on 28 May, and it corresponds to the most disturbed geomagnetic conditions. Ionospheric scatter during this interval consists of separated short-lived structures (with duration of 5–20 min), which localized along with the slant range and geomagnetic latitude. A specific shape of these structures indicates that the localized irregularities, associated with them, firstly moved toward the radar and then away from the radar. Doppler velocity varies in the range from −300 to 300 m/s, spectral widths is from ~100 to 250 m/s, and SNR is up to 35 dB. The slant range varies from 700 to 1,600 km, and latitude changes in the range from ~58.5° to ~66° MLAT. The lowest geomagnetic latitude was ~58.5° MLAT and observed at 02:00 UT, and then it moved poleward to ~66° MLAT at 05:30 UT. This interval is characterized by a strong absorption, sharp changes in foEs and fmin, including the periods of the complete blackout according to the riometer data in Amderma.

As seen from Figure 4f, starting from 23 UT on 27 May and till 18 UT on 28 May, there are only the Es traces identified according to the vertical sounding at Amderma. Note that foEs becomes stable and constant at ~2.8 MHz from 02:30 till 09:30 UT on 28 May. An absorption was practically at a quiet day level after 03 UT with a small increase up to 0.5 dB during 04–06 UT (Figure 4c). Starting from 05:30 UT, intensive ionospheric echoes were not registered by the EKB radar. However, we should note a weak ionospheric scatter during the interval 08:30–10:00 UT that occurred far from the radar at ~66° MLAT. Another weak scatter also appeared from 13:00 till 17:00 UT immediately near the radar at ~56–58° MLAT. These scatter appearance intervals are consistent with the increases in the foEs variations derived from the Amderma vertical sounding station.

Generally, the comparison of the Amderma riometer data and the EKB HF radar data shows a good agreement between the time periods of the increased riometer absorption and radar signals loss. This supports a more correct interpretation of the radar data obtained: The reflections are not absent, but due to high radio waves absorption in the lower ionosphere signals could not be detected by radar. However, we note that there is some time shift between the Amderma riometer absorption bays and the moments of the HF radar signals attenuation. This is caused by the difference in location of the regions where the absorption was measured and the HF echoes come from. At most of the moments, when the EKB radar registered intensive ionospheric echoes, they coincided with the moments when we observed intensive and relatively fast changes of foEs. However, that was not always observed, and the relationship between these parameters requires further investigation. The similar patterns of the ionospheric scatter development were also seen for other radar beams. The patterns were shifted in time and in a slant range (latitude).

Figure 4g shows the latitude-time-velocity plot for the Beam #12 (Ch. #1), which was directed to Norilsk. Time resolution for this beam is six times lower (about 2 min); therefore, the scatter pattern is less distinct. From this figure, we can see that intensive ionospheric echoes are observed from 22:30 on 27 May till 03:30 UT on 28 May over a latitudinal range from 57° to 64° MLAT. There are also weak echoes seen from 08:30 till 09:30 UT at ~60° MLAT and from 13:00 till 15:30 UT at ~56° MLAT.

To understand how the ionospheric irregularities were developed and moved in the EKB HF radar field of view, we mapped each echo to the geographical grid for each sounding time moment and each beam in Ch. #1. The result is presented in Movie S2 in the supporting information. In general, the ground scatter echoes come from the Kara Sea and the island of Novaya Zemlya. The ionospheric coherent scatters are localized in the region from 55°N to 80°N geographic longitude and from 58° to 66° MLAT. They moved continuously in the eastward direction during the period from ~18:00 UT on 27 May to ~05:30 UT on 28 May 2017.

4.3. Occurrence and Temporal Evolution of Ionospheric Irregularities—GPS ROT/ROTI

We processed the GPS observations from several available dual-frequency GPS receivers to obtain ROT and ROTI values as a measure of ionospheric irregularities impact on the received GPS radio signals. GPS ROT can characterize magnitude of GPS phase fluctuations related with rapid changes of the measured TEC along line of sight. Figure 5 presents GPS ROT variations for selected GPS stations during 27–28 May 2017. Each graph contains information about 18–06 MLT (magnetic local time); however, all stations located poleward of 60° MLAT (magnetic latitude) were in the conditions of the polar daylight ionosphere. In the absence of ionospheric irregularities, the GPS ROT slightly varies near the zero value within a narrow range of ±0.5–1.0 TECU/min (1 TECU = 10^{16} el/m^2); on the graph, it looks like a smooth horizontal line over a whole period of time when GPS satellite was visible. Before the storm onset at 15:34 UT on 27 May 2017, all stations were characterized by such a low level of the GPS ROT variability. As a station located most poleward (69.39° MLAT) from the considered set, DIKS experienced first significant phase fluctuations (ROT exceeded ±2–5 TECU/min) starting from 16 to 17 UT on 27 May 2017 (Figure 5a) during the initial phase of the storm when the AE index increased to ~400 nT. All GPS stations located poleward from 60° MLAT were affected by strong ionospheric irregularities starting from 22 to 23 UT when the auroral activity enhanced and the AE index rose up to ~1,500 nT. At that time, intense ionospheric irregularities were registered for all visible satellites at the more southward station SALE (~63° MLAT, Figure 5b). We note that an equatorward expansion of auroral irregularities toward midlatitudes did not reach 55° MLAT in the Siberian region. NOVM station (Figure 5c) showed very low GPS ROT variations of the similar magnitude before and during the geomagnetic storm. The similar behavior was observed at two other midlatitudinal stations ARTU (56.4°N, 58.6°E; 53° MLAT) and IRKM (52.2°N, 104.3°E; 48° MLAT) (not shown here).

Figures 5d–5f present GPS ROT variations for stations NRIL, SEYA, and AMDE located at similar latitude (~66° MLAT) within a longitudinal range of 60–90°E. Despite such a longitudinal difference, GPS observations for these stations revealed a quite similar behavior—a similar period of the phase fluctuation intensification (ROT exceeded ±3–5 TECU/min) from 22–23 UT on 27 May till ~03 UT on 28 May with a clear intensity decrease near 03–04 UT. After the period of the intensity decrease, intense phase fluctuations were registered at the NRIL station starting from ~05:30 UT on 28 May.

Movie S3 in the supporting information shows a spatiotemporal dynamics of the ionospheric irregularities occurrence as they are seen in the GPS ROTI observations. The GPS ROTI values were geolocated to IPPs (ionospheric pierce points) at 350-km altitude. The first intense irregularities were registered during 16–17 UT on 27 May for GPS satellites overpasses with IPPs within 70–80°N. After 22 UT, period of the enhanced activity in the irregularities occurrence was observed over the whole region. At 22:30–23:30 UT, a zone of intense irregularities (ROTI exceeded 1–2 TECU/min) expanded equatorward and reached 65–66°N (~62° MLAT) over a broad area of 50–100°E. At 03:00–04:30 UT on 28 May 2017, the magnitude of the ROTI variations was substantially decreased; they were observed mainly within a narrow belt of 65–70°N. Starting from 04:30 UT, the second intense irregularities were registered mainly close to the Norilsk location. These irregularities expanded continuously westward and equatorward until 10:00–11:00 UT when a zone of intense irregularities, narrow in latitudes (67–75°N), extended broadly over 50–100°E. This period of second strong intensification of ionospheric irregularities occurrence is well seen on Figures 5d–5f for the three well-separated GPS stations.

4.4. Storm-Time Evolution of the R1 and R2 FACs System

As a parameter of the magnetosphere-ionosphere coupling, we used AMPERE data of FAC spatial and temporal variability. Figure 6 shows the radial current density distribution as a function of time (UT) and geomagnetic latitude for two fixed longitudes at Amderma and Norilsk locations. Figure 6 illustrates behavior of the Region 1 (R1) and Region 2 (R2) FACs under the quiet and storm-time conditions during 27–28 May.

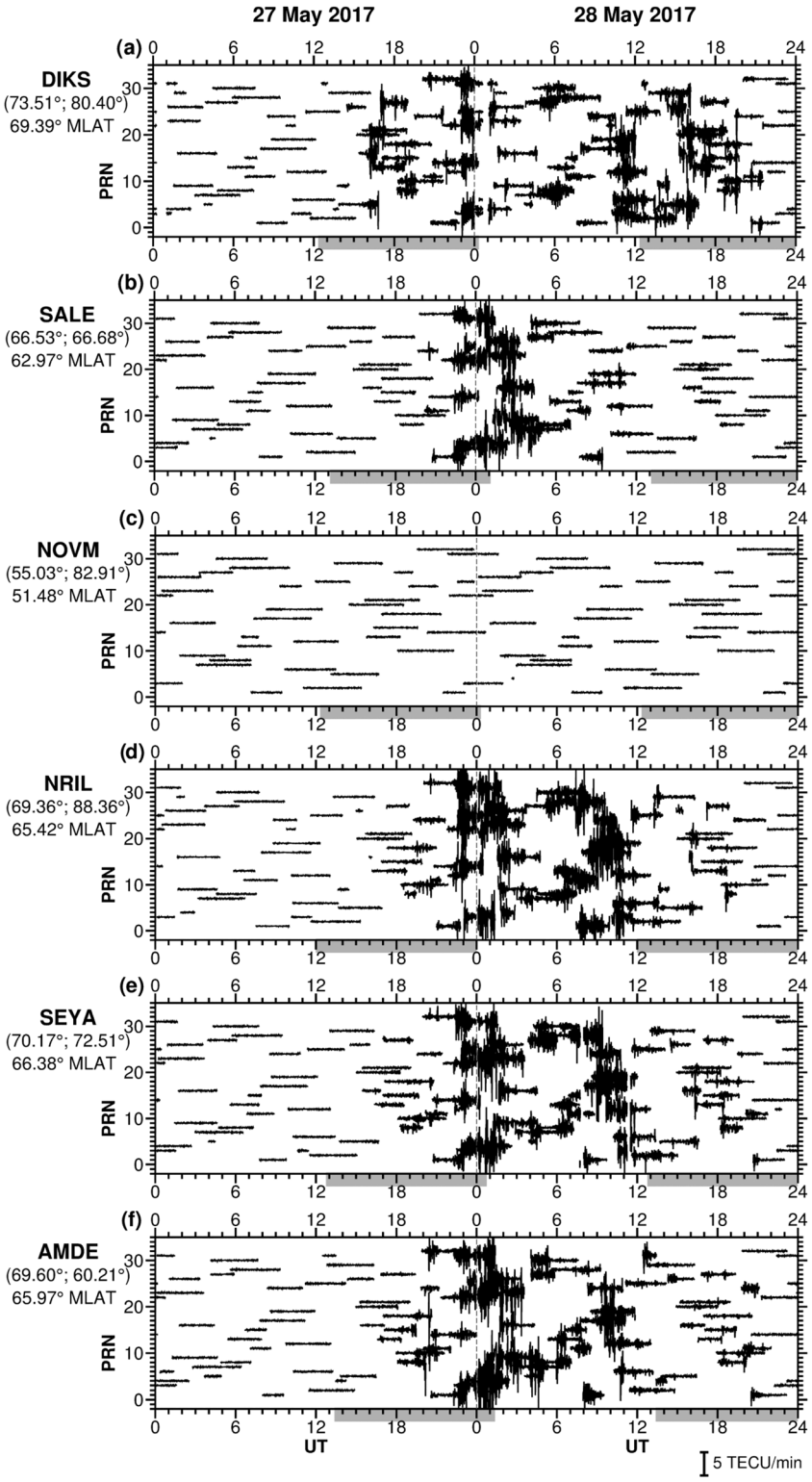

Figure 5. GPS ROT variations along all visible GPS satellites for selected ground-based GPS stations during 27–28 May 2017. Left axis shows PRN of GPS satellites, bottom—time in UT. Gray shadow below each graph shows 18–06 MLT conditions.

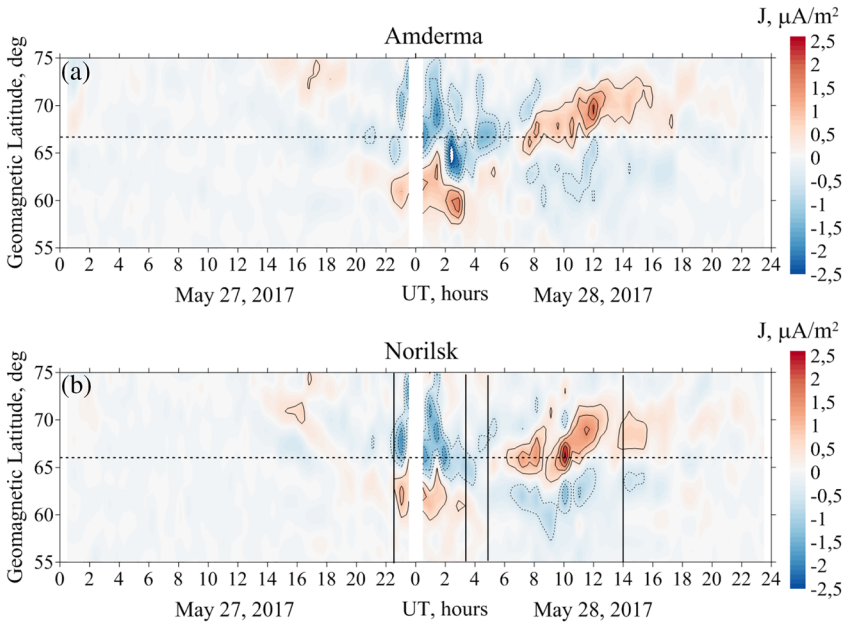

Figure 6. Map of the temporal distribution of the radial current density of FACs as derived for a fixed geomagnetic longitude at (a) Amderma and (b) Norilsk over the range of geomagnetic latitudes from 55° to 75°. The dashed black line shows the Amderma and Norilsk positions at geomagnetic latitudes of 66.7° and 66.0°, respectively. The currents directed away from the ionosphere are shown in red (positive values) and solid contours, and the currents flowing into the ionosphere—in blue (negative values) and dotted contours. Vertical lines in the panel (b) show time intervals of the UHF radar aurora appearance and disappearance according to Figure 3.

Two main differences in the magnetosphere-ionosphere currents system between the quiet and disturbed geomagnetic conditions can be recognized: (1) The FACs magnitudes were much smaller during quiet period; (2) the FACs regions located more poleward, near 75° MLAT for quiet condition in comparison to storm-time (near 60° MLAT). After 15:30 UT on 27 May, when a rapid increase in the solar wind speed was registered (Figure 1), we observe an increase in the R1 FAC intensity to 0.7 $\mu A/m^2$. At that time, an equatorward displacement of the R1 and R2 FACs zones was started. We should note that this period corresponded to 22–24 MLT, when the Harang discontinuity associated with the auroral ionospheric currents system is usually observed near local midnight. During 18:30–19:30 UT on 27 May 2017, a current flow reversal was registered at both longitudes of Amderma and Norilsk. There is quite a good relation between the FAC system behavior and the AE index variations during initial period of main storm phase as seen from comparison of Figures 1 and 6. After ~22 UT on 27 May, we note an intensification of the FACs at both Amderma and Norilsk longitudes that agreed well with a rapid AE index increase to ~1,500–1,700 nT during 22:00–03:00 UT. During this period, the zone of the upward R2 FAC shifted equatorward down to ~60° MLAT. At Amderma longitude, the R1 and R2 FACs zones drifted to much lower latitudes (~63° and 57° MLAT, respectively). After that, there is no such an obvious relation between the FACs behavior and the AE index variability. The peak FACs values (~2.0–2.5 $\mu A/m^2$) were observed at Norilsk and Amderma longitudes till ~04:00 UT on 28 May. For Norilsk longitude, the R1 and R2 FACs are extremely low (almost were not detected) from 04:00 till 05:00 UT on 28 May, and a prolonged reversal of the currents took place at that time. Over Amderma, the FACs intensity was weakening from 04:00 UT to 06:00 UT, and the zones shifted toward the pole. The FACs are practically absent during 06:00–07:00 UT on 28 May. After that period of the FACs low intensity and reversal, the R1 and R2 FACs intensified at both longitudes and shifted equatorward during 07:00–11:00 UT on 28 May. For Norilsk longitude, the current system was more developed; that is, an intensity of the downward FAC (in absolute values) was two times larger than those of Amderma longitude. During the storm's recovery phase, an equatorward border of the FAC zones located at rather low latitudes, and it returned to the pre-storm conditions only after ~18 UT on 28 May 2017.

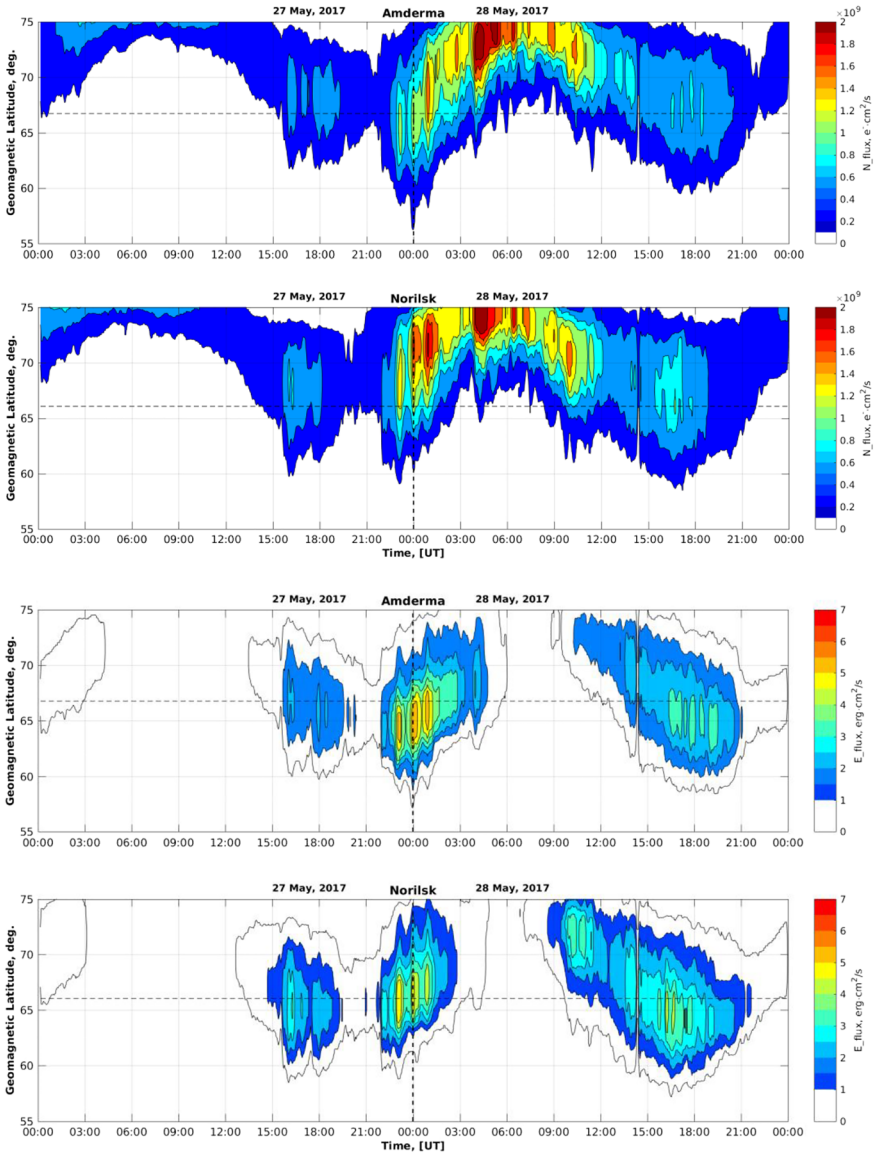

Figure 7. Auroral precipitations predicted by the modified OVATION Prime model. The E-flux of precipitated particles (ions plus electrons) are presented on top two panels for Amderma and Norilsk geomagnetic longitudes. The same plots for N-flux are presented on the bottom. The horizontal dashed lines denote geomagnetic latitudes of Amderma and Norilsk, respectively. Vertical dashed lines divide 27 and 28 May 2017.

4.5. Energy and Fluxes of High-Energy Auroral Particle Precipitation

Figure 7 shows geomagnetic latitude-time spectrograms of energy and number fluxes for Amderma and Norilsk geomagnetic longitudes as obtained from the PC index version of the OP-2010. On the two upper panels of Figure 7, a sum of energy flux (E-flux) of discrete/diffuse electrons and diffuse ions with energy less than 30 keV are marked with color. The lower two panels of Figure 7 in turn represent their number flux (N-flux). The horizontal dashed lines denote geomagnetic latitudes of Amderma and Norilsk consequently. Detailed dynamics of auroral precipitation is compiled and presented in Movie S4 in the supporting information. The equatorial boundary of the visible aurora in the model is defined with fixed electron energy flux threshold, which was chosen as 1 erg cm^{-2} s^{1} (Kivelson & Russell, 1995; Machol et al., 2012).

Despite the fact that the OVATION Prime is an empirical model driving by PC index, a behavior of predicted auroral precipitations is similar to in situ measurements of ionospheric FAC deduced from the AMPERE experiment. The beginning of strong energetic auroral precipitation coincide with the AMPERE FACs

appearing at ~22 UT on 27 May. After that precipitation region was shifting to the North, and at 03 UT on 28 May E-flux becomes negligible while N-flux, on the contrary, becomes maximum on latitudes 70° and higher. It indicates that at this time magnetic local time became noon and only soft electron and ion precipitations from the cusp region exist. OP-2010 calculations coincide with the FAC estimation which shows that at this time currents system started to change from premidnight to postmidnight (Region 2 FAC changed from upward to downward). After current system reversal till 12 UT of 28 May, a precipitation region moves equatorward similarly to the FAC deduced by AMPERE data.

5. Discussion

5.1. Similarities and Differences Between Auroral Backscatter and GPS ROT Behavior

Despite diversity in scales of the ionospheric irregularities revealed in the ROT based on GPS measurements corresponding to L band, and HF/UHF radar backscatter, they have distinct similarities. A combined analysis of temporal characteristics of auroral backscatter and ROT revealed their simultaneous appearance: (1) for the GPS station NRIL located in the same latitudinal and longitudinal range as the UHF radar field of view; (2) for the GPS stations AMDE and SALE located in the same latitudinal and longitudinal range as the HF radar field of view. Clear examples of such similarities are the following: (1) most distinct signatures of UHF and HF radar aurora with its most equatorward location during time periods of 22:30 UT on 27 May till 02:00 UT on 28 May and 08:00–11:00 UT on 28 May simultaneously with the GPS ROT largest increase at Norilsk, Salekhard, and Amderma GPS receivers; (2) UHF and HF backscatter have been disappeared synchronously with a significant decrease in the GPS ROT over Norilsk during 03:30–05:00 UT on 28 May; and (3) a westward expansion of radar aurora and disturbances in GPS ROT during 05–08 UT on 28 May. The GPS stations DIKS and NOVM stations are located poleward and equatorward of the radar's field of view, respectively; thus, their ROT behavior was quite different.

5.2. Comparison of HF and UHF Backscatter Radar Aurora

We have an opportunity to simultaneously consider HF and UHF radar aurora development using Figures 3 and 4, as well as Movies S1 and S2 in the supporting information. The joint analyses of these observations both extend our vision on the occurrence and development of ionospheric irregularities during geomagnetic storm on 27–28 May 2019 and provide information regarding similar and different features of HF and UHF radar aurora. One of the factors influencing on the difference of HF and UHF backscatter signatures is the spatial diversity of the radars and their fields of view (see Figure 2). Due to more western location of HF radar field of view in comparison to UHF radar, we firstly revealed occurrence of HF radar aurora on the Amderma direction at 18:30 UT on 27 May 2019 (see Figure 4 and Movie S2 in the supporting information). HF radar aurora was periodically developing until 22:30 UT on 27 May, continuously shifting eastward. A simultaneous detection of strong irregularities appeared at approximately 22:30 UT on 27 May as seen by UHF radar (Figure 3) and HF radar at the Beam #12 directed toward Norilsk (Figure 4g). The irregularities were observed at both radars until 03:30 UT on 28 May. During this period (22:30 UT on May 27 to 03:30 UT on May 28) according to HF radar, the observed Doppler drift velocities were increasing significantly (up to 300 m/s), and the region of ionospheric irregularities according to HF and UHF radar data were shifting eastward (see Movies S1 and S2).

Degradation of HF backscatter at the Beam #2 directed to Amderma during the period 00:00–02:00 UT on 28 May is explained by significant absorption that supported by riometer observations (see Figure 4c). At the same time interval, the sporadic E layer was strongly developing over Amderma. Both these facts associated with equatorward expansion of high-energy particle precipitation that occurred during 00:00–02:00 UT on 28 May (see Figures 7a and 7c). The same situation appeared for HF radar at the Beam #12 directed toward Norilsk during time interval from 00:30 until 03:30 on 28 May when the significant Doppler velocity observed together with decreasing of HF radar aurora intensity. During that period UHF radar aurora was developing strongly as seen in Figure 3.

Considering that signals in the UHF band are almost non-sensitive to atmospheric absorption rather than in HF band, we can conclude that time interval of UHF and HF backscatter (Beam #12 directed toward Norilsk) absence from 03:30 till 05:00 UT on 28 May is related to the disappearance of ionospheric irregularities associated mainly with FACs attenuation (see section 5.3 for more detail). It is necessary to take into account that the EKB radar mode switched to twice per hour from 04 UT on 28 May. Therefore,

we cannot consider the relation of HF and UHF radar data during 05:00–14:00 UT when strong developed and westward expanded UHF radar aurora was observing.

According to radars location (Figure 2), HF backscatter was observed at a near zero aspect angle rather than UHF backscatter observed at large aspect angles. Radar reflections from E layer irregularities observed at directions around near zero aspect angles are well explained by linear theory of the gradient-drift and two-stream instabilities. However, there are many cases where coherent backscatter observed at large aspect angle (e.g., Jackel et al., 1997; Moorcroft, 1996). An appropriate nonlinear theory was discussed by Hamza (1992) and Hamza and St-Maurice (1995).

5.3. Impact of FACs and Particle Precipitation on Multi-scale Ionospheric Irregularities Formation, Transport, and Variability

We compared time periods of the ionospheric irregularities detection by different instruments with spatio-temporal changes of the R1 and R2 FACs and particles precipitation. The time interval of the equatorward displacement and intensification of the R1 and R2 FACs that occurred during considered geomagnetic storm (see Figure 6) is correlated with the UHF radar aurora existence from 22:30 UT on 27 May till 14:00 UT on 28 May (see Figures 3a and 3b). Appearance of UHF backscatter is consistent with a period of FAC intensification at Norilsk longitude (up to 2.0–2.5 $\mu A/m^2$). During time interval from 22:30 UT on 27 May until 03:30 UT on 28 May, the UHF radar aurora located at latitudes of upward R2 FAC and on 2–3° equatorward which is in agreement with previous results (Waters et al., 2001) and data from Figure 7 associated with downward precipitating electrons. During the same time interval, the similar conclusion can be made according to comparison of temporal evaluation and latitudinal displacement of HF radar aurora and R2 FAC.

Figures 3 and 4g revealed a disappearance of UHF and HF (Beam #12 toward Norilsk) aurora backscatter during 03:30–05:00 UT on 28 May 2017. The absence of HF radar aurora was prolonging until 08:00 UT due to more southern location of HF radar field of view in comparison to UHF radar one. There was a decrease of GPS ROT over Norilsk at the same time interval (03:30–05:00 UT on 28 May) (Figure 5). The similar situation observed at Amderma direction where synchronous absence of HF auroral backscatter and a decrease of GPS ROT were revealed during 05:30–09:00 UT on 28 May. These phenomena are most likely related to a decrease of ionospheric electric field due to a decrease of FACs that observed during this period (see Figure 6). In addition at the same time, according to Figure 7, a high-energy auroral precipitation was almost disappeared that possibly led to a decrease of the E region electron density and related disappearance of E region ionospheric irregularities. Such relations of different parameters are in good agreement with previous results that revealed a significant dependence of radar aurora on electric field, auroral electrojet, and E region electron density (e.g., Hysell et al., 2012; Koustov et al., 1989; Starkov et al., 1983; Uspensky et al., 1989). A significant role of the FAC system development for ionospheric irregularities formation is evident also from the comparison of GPS ROTI and FACs over Norilsk and Amderma during 08:00–11:00 UT on 28 May 2017. There is a clear enhancement of the GPS ROTI over Norilsk and Amderma approximately coinciding with increase of FACs intensity. The GPS ROTI variations over Norilsk were much larger than those over Amderma due to the corresponding relation with the R2 FAC. In addition, temporal variability of the latitudinal location of R2 FAC at Norilsk longitude is consisted to variability of equatorial boundary of UHF radar aurora. Also, we note that during the aforementioned period the UHF radio aurora observed in the entire azimuthal field of view (see Movie S1).

It is important that at the storm main phase, the substantial equatorward expansion of the irregularities as observed by GPS receivers, UHF and HF radars followed after similar dynamics of FACs and auroral particle precipitation. Disappearance of UHF and HF auroral backscatter during 03:30–05:00 UT on 28 May 2017 and decrease of GPS ROTI over Norilsk are most likely related to a decrease of FACs intensity during a near noon prolonged reversal of R1 and R2 FAC directions. Combined analysis revealed that area of intense irregularities is connected and located equatorward to the low-latitude boundary of the auroral oval and FACs at different stages of geomagnetic storm. This conclusion is in a good agreement with previous results (e.g., Greenwald et al., 1973; Sahr & Farley, 1996). Aforementioned feature can be explained by intensification of ionospheric electric field equatorward to upward/downward FACs that is shown by abovementioned combined analysis of FACs and Doppler velocity presented on Figures 4 and 6. Such intensified electric field leads to a development of Farley-Buneman and gradient-drift instabilities. We revealed that different structures of FAC system lead to different zonal drift direction of ionospheric irregularities. This could be

considered as additional proof of FAC influence on the irregularities. At the first interval (18:30 UT on 27 May to 03:30 UT on 28 May for HF radar; 22:30 UT on 27 May to 03:30 UT on 28 May for UHF radar), there are (1) eastward drift of irregularities (see Movies S1–S3) and (2) downward R1 FAC and upward R2 FAC (see Figure 6). Such configuration of R1 and R2 FAC should lead to existence of southward electric field component (eastward plasma drift) at auroral and subauroral region. After reversal of R1 and R2 FAC directions during 05:00–14:00 UT on 28 May (see Figure 6), the northward component of electric field is formed that explained the westward drift of irregularities observed by UHF radar (see Movie S1).

According to Kelley (2009), in the MLT sector of the R2 FAC emanating from the ionosphere, an eastward electric field is formed at the middle and subauroral latitudes, which means the poleward and upward $E \times B$ plasma drift. This situation takes place in the Norilsk longitude from 22:30 UT on 27 May to 03:30 UT on 28 May. Near noon MLT from 03:30 to 05:30 UT at the Norilsk longitude the FAC system is reconfigured that leads to the change of directions of the horizontal and vertical components of the $E \times B$ plasma drift. Then the current structure becomes opposite to first temporal block, which according to Kelley (2009) leads to the formation of a westward electric field and the downward and equatorward ionospheric plasma drift including irregularities transport. Such FACs configuration exists on 28 May from 05:30 to 14:00 UT. This is the main reason for the differences of heights of the observed ionospheric irregularities between the first and second temporal block of UHF radar backscatter. Thus, we revealed that R1/R2 FAC system influences to irregularities formation and variability: (1) Increase and equatorward displacement of R1/R2 FACs leads to appearance and equatorward expansion of ionospheric irregularities; (2) degradation of R1 and R2 FACs during near noon FAC system reversal leads to disappearance of ionospheric irregularities; and (3) during downward (upward) R1 FAC and upward (downward) R2 FAC, the eastward and upward (westward and downward) drift of ionospheric irregularities occurred.

6. Summary

In this work, we present results of the multi-instrumental study of ionospheric irregularities of different scales observed over the Central and East Siberian region of Russia during the geomagnetic storm on 27–28 May 2017. This storm provided us with a great opportunity to investigate ionospheric irregularities by using a set of instruments with large longitudinal coverage. One of advantages of UHF radar and GPS techniques is that they trace behavior of irregularities during the storm without being affected by strong absorption.

The main results of this study can be summarized as follows:

1. For the first time, a strong agreement between the GPS ROT and UHF/HF auroral backscatter was revealed for both spatial and temporal domains (except of a period of strong absorption at the HF band). We found a correlation between different-scale ionospheric irregularities during initial, main, and recovery phases of the geomagnetic storm.
2. Increase of R1/R2 FACs leads to an appearance of ionospheric irregularities possibly through enhancement of horizontal electric field in the auroral and subauroral regions. At the storm main phase, the substantial equatorward expansion of the multi-scale irregularities, as observed by the UHF/HF radars, followed after similar dynamics of FACs and auroral oval (particle precipitation).
3. Disappearances of the UHF and HF auroral backscatters during 03:30–05:00 UT and 03:30–08:00 UT on 28 May 2017, respectively, were coincided with a decrease of GPS ROT over Norilsk. The similar situation observed at Amderma direction where synchronous absence of HF auroral backscatter and a decrease of GPS ROT were revealed during 05:30–09:00 UT on 28 May. We consider these phenomena are most likely related to a decrease of FACs intensity during a prolonged near noon reversal of R1 and R2 FAC directions.
4. We found that R1/R2 FAC system influences to ionospheric irregularities transport. During downward (upward) R1 FAC and upward (downward) R2 FAC, the eastward and upward (westward and downward) drift of ionospheric irregularities occurred.

These results demonstrate a high effectivity and capability of the proposed set of the ground-based radiophysical instruments together with research payloads onboard multi-satellite systems for basic research and operational monitoring of the ionospheric irregularities at high-latitude regions around the globe.

Acknowledgments

We acknowledge the use of GPS data provided by IGS (ftp://cddis.gsfc.nasa.gov). We thank the AMPERE team and AMPERE Science Center for providing Iridium-derived data products. AMPERE data are available online (via http://ampere.jhuapl.edu. We thank NASA/GSFC's Space Physics Data Facility's OMNIWeb service (https://omniweb.gsfc.nasa.gov/ow_min.html). All other data will be available online (at DOI:10.5281/zenodo.3731320). Works of V. Ovodenko, M. Klimenko, I. Zakharenkova, D. Kotova, D. Chugunin, and A. Chernyshov with morphology of different-scale ionospheric irregularities and its explanation were supported by the Russian Science Foundation Grant 17-77-20009. The reported study of auroral particle precipitation performed by A. Nikolaev and D. Rogov was funded by RFBR Project 18-05-80004. Daria Kotova was partially supported by the Research Council of Norway, Grant 267408. The work of A. Oinats and K. Ratovsky was performed with budgetary funding of Basic Research program II.12. The EKB HF radar observational results were obtained using the equipment of Center for Common Use «Angara» (http://ckp-rf.ru/ckp/3056/).

References

Aarons, J., & Lin, B. (1999). Development of high latitude phase fluctuations during the January 10, April 10-11, and May 15, 1997 magnetic storms. *Journal of Atmospheric and Solar Terrestrial Physics*, *61*(3-4), 309–327. https://doi.org/10.1016/s1364-6826(98)00131-x

Anderson, B. J., Korth, H., Waters, C. L., Green, D. L., Merkin, V. G., Barnes, R. J., & Dyrud, L. P. (2014). Development of large-scale Birkeland currents determined from the active magnetosphere and planetary electrodynamics response experiment. *Geophysical Research Letters*, *41*, 3017–3025. https://doi.org/10.1002/2014GL059941

Bagaryatsky, B. A. (1961). Radar reflections from aurorae. *Uspekhi fizicheskikh nauk [Soviet Physics–Uspekhi]*, *73*(2), 197–241. Placeholder Text(In Russian). https://doi.org/10.3367/UFNr.0073.196102a.0197

Bahcivan, H., Hysell, D. L., Lummerzheim, D., Larsen, M. F., & Pfaff, R. F. (2006). Observations of colocated optical and radar aurora. *Journal of Geophysical Research*, *111*, A12308. https://doi.org/10.1029/2006JA011923

Bilitza, D., Altadill, D., Zhang, Y., Mertens, C., Truhlik, V., Richards, P., et al. (2014). The International Reference Ionosphere 2012—A model of international collaboration. *Journal of Space Weather and Space Climate*, *4*(A07), 1–12. https://doi.org/10.1051/swsc/2014004

Blanchard, G. T., Sundeen, S., & Baker, K. B. (2009). Probabilistic identification of high-frequency radar backscatter from the ground and ionosphere based on spectral characteristics. *Radio Science*, *44*(5), RS5012. https://doi.org/10.1029/2009RS004141

Buneman, O. (1963). Excitation of field-aligned sound waves by electrons streams. *Physical Review Letters*, *10*(7), 285–287. https://doi.org/10.1103/physrevlett.10.285

Cherniak, I., Zakharenkova, I., & Redmon, R. J. (2015). Dynamics of the high-latitude ionospheric irregularities during the 17 March 2015 St. Patrick's Day storm: Ground-based GPS measurements. *Space Weather*, *13*(9), 585–597. https://doi.org/10.1002/2015SW001237

Cherniak, I., Zakharenkova, I., & Sokolovsky, S. (2019). Multi-instrumental observation of storm-induced ionospheric plasma bubbles at equatorial and middle latitudes. *Journal of Geophysical Research: Space Physics*, *124*, 1491–1508. https://doi.org/10.1029/2018JA026309

Chisham, G., & Freeman, M. P. (2013). A reassessment of SuperDARN meteor echoes from the upper mesosphere and lower thermosphere. *Journal of Atmospheric and Solar - Terrestrial Physics*, *102*, 207–221. https://doi.org/10.1016/j.jastp.2013.05.018

Chisham, G., Lester, M., Milan, S. E., Freeman, M. P., Bristow, W. A., Grocott, A., et al. (2007). A decade of the Super Dual Auroral Radar Network (SuperDARN): Scientific achievements, new techniques and future directions. *Surveys in Geophysics*, *28*(1), 33–109. https://doi.org/10.1007/s10,712-007-9017-8

Cole, K. D. (1963). Motions of the aurora and radio-aurora and their relationships to ionospheric currents. *Planetary and Space Science*, *10*, 129–163. https://doi.org/10.1016/0032-0633(63)90013-8

Coxon, J. C., Milan, S. E., & Anderson, B. J. (2018). A review of Birkeland current research using AMPERE. *Geophysical Monograph Series*, 257–278. https://doi.org/10.1002/9781119324522.ch16

Evans, D. S. (1987). Global statistical patterns of auroral phenomena. In Y. Kamide, & R. A. Wolf (Eds.), *Proceedings of Quantitative modeling of magnetospheric-ionospheric coupling processes* (pp. 325–330). Kyoto, Japan: Kyoto Sangyo Univ.

Farley, D. T. (1963). A plasma instability resulting in field-aligned irregularities in the ionosphere. *Journal of Geophysical Research*, *68*(22), 6083–6097. https://doi.org/10.1029/jz068i022p06083

Fejer, B. G., & Kelley, M. C. (1980). Ionospheric irregularities. *Reviews of Geophysics and Space Physics*, *18*(2), 401–454. https://doi.org/10.1029/rg018i002p00401

Foster, J. C., & Tetenbaum, D. (1991). High-resolution backscatter power observations of 440-Mhz E region coherent echoes at Millstone Hill. *Journal of Geophysical Research*, *96*(A2), 1251–1260. https://doi.org/10.1029/90JA02179

Greenwald, R. A. (1996). Chapter 13. The role of coherent radars in ionospheric and magnetospheric research. In H. Kohl, R. Rüster, & K. Schlegel (Eds.), *Modern ionospheric science*, (pp. 391–414). Lindau, Germany: Max-Planck Institut fur Aeronomie.

Greenwald, R. A., Ecklund, W. L., & Balsley, B. B. (1973). Auroral currents, irregularities and luminosity. *Journal of Geophysical Research*, *78*(34), 8193–8203. https://doi.org/10.1029/ja078i034p08193

Gustafson, G., Sverdlov, Y. L., & Sergeyeva, H. G. (1980). *Struktura avroral'noy subburi [Rezu1'taty MIM] [Structure of the auroral substorm (MIM results)]*, (p. 54). Apatity, 1980: Press of Kola Branch, USSR Acad. Sci.

Haldoupis, C. (1989). A review on radio studies of auroral E-region ionospheric irregularities. *Annales de Geophysique*, *7*, 239–258.

Hamza, A. M. (1992). A non-linear theory for large aspect angle echoes in the auroral E region. *Journal of Geophysical Research*, *97*(A11), 16,981–16,993. https://doi.org/10.1029/92JA00836

Hamza, A. M., & St-Maurice, J.-P. (1995). Large aspect angles in auroral E region echoes: A self-consistent turbulent fluid theory. *Journal of Geophysical Research*, *100*(A4), 5723–5732. https://doi.org/10.1029/94JA03026

Hanuise, C. (1983). High latitude irregularities: A review of recent radar results. *Radio Science*, *18*(6), 1093–1121. https://doi.org/10.1029/rs018i006p01093

Hardy, D. A., Gussenhoven, M. S., & Brautigan, D. (1989). A statistical model of ion precipitation. *Journal of Geophysical Research*, *94*(A1), 370. https://doi.org/10.1029/ja094ia01p00370

Hardy, D. A., Gussenhoven, M. S., & Holeman, E. (1985). A statistical model of auroral electron precipitation. *Journal of Geophysical Research*, *90*(A5), 4229. https://doi.org/10.1029/JA090iA05p04229

Hysell, D., Miceli, R., Munk, J., Hampton, D., Heinselman, C., Nicolls, M., et al. (2012). Comparing VHF coherent scatter from the radar aurora with incoherent scatter and all-sky auroral imagery. *Journal of Geophysical Research*, *117*, A10313. https://doi.org/10.1029/2012JA018010

Hysell, D. L. (2015). The radar aurora. *Auroral Dynamics and Space Weather*, 191–209. https://doi.org/10.1002/9781118978719.ch14

Jackel, B. J., Moorcroft, D. R., & Schlegel, K. (1997). Characteristics of very large aspect angle E-region coherent echoes at 933 MHz. *Annales de Geophysique*, *15*(1), 54–62. https://doi.org/10.1007/s00585-997-0054-x

Jakowski, N., Béniguel, Y., De Franceschi, G., Hernández-Pajares, M., Jacobsen, K. S., Stanislawska, I., & Wautelet, G. (2012). Monitoring, tracking and forecasting ionospheric perturbations using GNSS techniques. *Journal of Space Weather and Space Climate*, *2*, A22. https://doi.org/10.1051/swsc/2012022

Jayachandran, P. T., Donovan, E. F., MacDougall, J. W., Moorcroft, D. R., St. Maurice, J.-P., & Prikryl, P. (2002). SuperDARN E-region backscatter boundary in the dusk-midnight sector—Tracer of equatorward boundary of the auroral oval. *Annales de Geophysique*, *20*(12), 1899–1904. https://doi.org/10.5194/angeo-20-1899-2002

Jayachandran, P. T., St.-Maurice, J.-P., MacDougall, J. W., & Moorcroft, D. R. (2000). HF detection of slow long-lived *E* region plasma structures. *Journal of Geophysical Research*, *105*(A2), 2425–2442. https://doi.org/10.1029/1999JA900367

Kamide, Y. (2013). On the empirical relationship between field-aligned currents and auroras. In S. Akasofu, & J. Kan (Eds.), *Physics of auroral arc formation*, *Geophysical Monograph Series* (p. 25). American Geophysical Union. https://doi.org/10.1029/GM025p0192

Kamide, Y., & Rostoker, G. (1976). The spatial relationship of field-aligned currents and auroral electrojets to the distribution of nightside auroras. *Journal of Geophysical Research*, *82*(35), 5589–5608. https://doi.org/10.1029/ja082i035p05589

Kelley, M. (2009). *The Earth's ionosphere. Plasma physics and electrodynamics* (2nd ed.). United States of America: Elsevier Publishing Company.

Kivelson, M. G., & Russell, C. T. (1995). *Introduction to space physics*. Cambridge, UK: Cambridge University Press.

Koustov, A., Uspensky, M., Kangas, J., Huuskonen, A., & Nielsen, E. (1989). On the threshold electric field for the ≈1-m auroral irregularity appearance. *Journal of Geophysical Research*, *94*(A9), 12,043–12,048. https://doi.org/10.1029/JA094iA09p12043

Kurkin, V. I., Kutelev, K. A., Oinats, A. V., & Nishitani, N. (2012). The outlook of SuperDARN radars application for monitoring of the ionospheric dynamics in Russia. *Physical Bases of Instrumentation*, *1*(3), 3–18. (in Russian) https://doi.org/10.25210/jfop-1203-003018

Leadabrand, R. L., Jaye, W. E., & Dyce, R. B. (1961). A note on 106.1-Mc auroral echoes detected at Stanford following the solar event of November 12, 1960. *Journal of Geophysical Research*, *66*(4), 1069–1072. https://doi.org/10.1029/JZ066i004p01069

Leadabrand, R. L., Larson, A. G., & Hodges, J. C. (1967). Preliminary results on the wavelength dependence and aspect sensitivity of radar auroral echoes between 50 and 3000 MHz. *Journal of Geophysical Research*, *72*(15), 3877–3887. https://doi.org/10.1029/JZ072i015p03877

Leadabrand, R. L., Schlobohm, J. C., & Baron, M. J. (1965). Simultaneous very high frequency and ultra high frequency observations of the aurora at Fraserburg, Scotland. *Journal of Geophysical Research*, *70*(17), 4235–4284. https://doi.org/10.1029/jz070i017p04235

Machol, J. L., Green, J. C., Redmon, R. J., Viereck, R. A., & Newell, P. T. (2012). Evaluation of OVATION prime as a forecast model for visible aurorae. *Space Weather*, *10*, S03005. https://doi.org/10.1029/2011SW000746

McDiarmid, D. R. (1976). On errors in the measurement of the aspect sensitivity of radio aurora. *Journal of Geophysical Research*, *81*(22), 4007–4009. https://doi.org/10.1029/ja081i022p04007

Moorcroft, D. R. (1996). A statistical study of UHF auroral backscatter at large magnetic aspect angle: A reanalysis of unpublished results from 1968. *Journal of Geophysical Research*, *101*(A5), 11,005–11,011. https://doi.org/10.1029/96JA00439

Murphy, K. R., Man, I. R., Jonathan Rae, I., Waters, C. L., Frey, H. U., Kale, A., et al. (2013). The detailed spatial structure of field aligned currents comprising the substorm current wedge. *Journal of Geophysical Research: Space Physics*, *118*(12), 7714–7727. https://doi.org/10.1002/2013JA018979

Newell, P. T., Sotirelis, T., Liou, K., Lee, A. R., Wing, S., Green, J., & Redmon, R. (2010). Predictive ability of four auroral precipitation models as evaluated using polar UVI images. *Space Weather*, *8*, S12004. https://doi.org/10.1029/2010SW000604

Newell, P. T., Sotirelis, T., & Wing, S. (2009). Diffuse, monoenergetic, and broadband aurora: The global precipitation budget. *Journal of Geophysical Research*, *114*, A09207. https://doi.org/10.1029/2009JA014326

Nishitani, N., Ruohoniemi, J. M., Lester, M., Baker, J. B. H., Koustov, A. V., Shepherd, S. G., et al. (2019). Review of the accomplishments of mid-latitude Super Dual Auroral Radar Network (SuperDARN) HF radars. *Progress in Earth and Planetary Science*, *6*(1), 27. https://doi.org/10.1186/s40645-019-0270-5

Oinats, A. V., Nishitani, N., Ponomarenko, P., & Ratovsky, K. (2016). Diurnal and seasonal behavior of the Hokkaido east SuperDARN ground backscatter: Simulation and observation. *Earth, Planets and Space*, *68*(1), 18. https://doi.org/10.1186/s40623-015-0378-9

Pi, X., Mannucci, A. J., Lindqwister, U. J., & Ho, C. M. (1997). Monitoring of global ionospheric irregularities using the worldwide GPS network. *Geophysical Research Letters*, *24*(18), 2283–2286. https://doi.org/10.1029/97GL02273

Prikryl, P., & Cogger, L. L. (1992). Statistical analysis of the spatial relationship between the radio and optical aurora: Further evidence for refraction. *Radio Science*, *27*(4), 469–479. https://doi.org/10.1029/92RS00570

Prikryl, P., Jayachandran, P. T., Mushini, S. C., & Richardson, I. G. (2014). High-latitude GPS phase scintillation and cycle slips during high-speed solar wind streams and interplanetary coronal mass ejections: A superposed epoch analysis. *Earth, Planets and Space*, *66*(1), 62. https://doi.org/10.1186/1880-5981-66-62

Prikryl, P., Weygand, J. M., Viljanen, A., Connors, M., Danskin, D. W., Jayachandran, P. T., et al. (2016). GPS phase scintillation at high latitudes during the geomagnetic storm of 17–18 March 2015. *Journal of Geophysical Research: Space Physics*, *121*, 10,448–10,465. https://doi.org/10.1002/2016JA023171

Rogister, A., & D'Angelo, N. (1970). Type 2 irregularities in the equatorial electrojet. *Journal of Geophysical Research*, *75*(19), 3879–3887. https://doi.org/10.1029/ja075i019p03879

Sahr, J., & Farley, D. (1996). Auroral electrojet plasma irregularity theory and experiment: A critical review of present understanding and future directions. *Journal of Geophysical Research*, *101*(A12), 26,893–26,909. https://doi.org/10.1029/96JA02404

Schlegel, K. (1996). Coherent backscatter from ionospheric E-region plasma irregularities. *Journal of Atmospheric and Terrestrial Physics*, *58*(8-9), 933–941. https://doi.org/10.1016/0021-9169(95)00124-7

Schlegel, K., & Gurevich, A. V. (1997). Radar backscatter from plasma irregularities of the lower E region induced by neutral turbulence. *Annales de Geophysique*, *15*(7), 870–877. https://doi.org/10.1007/s00585-997-0870-z

Starkov, G. V., Oksman, J., Uspensky, M. V., & Kustov, A. V. (1983). On the dependence of radar aurora amplitude on ionospheric electron density. *Journal of Geophysics*, *52*(1), 49–52.

Sverdlov, Y. L., Sergeyeva, N. G., & Voloshinov, N. N. (1979). Global'noe raspredelenie radioavrory i prodol'nye toki. *Geomagnetism and Aeronomy*, *19*(229), 755–758. (in Russian)

Troshichev, O. A., & Andrezen, V. G. (1985). The relationship between interplanetary quantities and magnetic activity in the southern polar cap. *Planetary and Space Science*, *33*(4), 415–419. https://doi.org/10.1016/0032-0633(85)90086-8

Troshichev, O. A., Andrezen, V. G., Vennerstrom, S., & Friis-Christensen, E. (1988). Magnetic activity in the polar cap—A new index. *Planetary and Space Science*, *36*(11), 1095–1102. https://doi.org/10.1016/0032-0633(88)90063-3

Tsunoda, R. T., & Presnell, R. I. (1976). On a threshold electric field associated with the 398 MHz diffuse aurora. *Journal of Geophysical Research*, *81*(1), 88–96. https://doi.org/10.1029/ja081i001p00088

Unwin, R. S. (1966). The morphology of the radio aurora at sunspot maximum, II. The behaviour of different echo types. *Journal of Atmospheric and Terrestrial Physics*, *28*(12), 1183–1194. https://doi.org/10.1016/s0021-9169(17)30065-x

Uspensky, M. V., Janhunen, P., Koustov, A. V., & Kauristie, K. (2011). Volume cross section of auroral radar backscatter and RMS plasma fluctuations inferred from coherent and incoherent scatter data: A response on backscatter volume parameters. *Annales de Geophysique*, *29*(6), 1081–1092. https://doi.org/10.5194/angeo-29-1081-2011

Uspensky, M. V., Starkov, G. V., Stepanov, G. S., & Williams, P. J. S. (1989). The amplitude of auroral backscatter: 2. Topology of the backscatter range-azimuth distribution. *Journal of Atmospheric and Terrestrial Physics*, *51*(11/12), 926–936. https://doi.org/10.1016/0021-9169(89)90008-1

Waters, C. L., Anderson, B. J., & Liou, K. (2001). Estimation of global field aligned currents using the iridium® system magnetometer data. *Geophysical Research Letters*, *28*(11), 2165–2168. https://doi.org/10.1029/2000GL012725